Approximating idealized hybrid rocket fuel port geometries using steps

Christopher Glaser, Jouke Hijlkema, Jérôme Anthoine

To cite this version:

Christopher Glaser, Jouke Hijlkema, Jérôme Anthoine. Approximating idealized hybrid rocket fuel port geometries using steps. Space Propulsion 2022, May 2022, Estoril, Portugal. hal-03910531

HAL Id: hal-03910531

https://hal.science/hal-03910531v1

Submitted on 22 Dec 2022

APPROXIMATING IDEALIZED HYBRID ROCKET FUEL PORT GEOMETRIES USING STEPS

Christopher Glaser (1),*, **Jouke Hijlkema** (1), **Jérôme Anthoine** (1)

(1) ONERA/DMPE, Université de Toulouse, F-31410 Mauzac, France
** E-mail: christopher.glaser@onera.fr*

KEYWORDS: Hybrid propulsion, stepped geometry, profile optimization, regression rate.

NOMENCLATURE:

ρ	Density
$\dot{\omega}$	Production rate
η	Radial coordinate
λ	Thermal conductivity
μ	Dynamic viscosity
A	Area
A_{pyr}	Arrhenius pre-exponent
c_p	Heat capacity
D	Diameter
D_m	Diffusion coefficient
E_a	Activation energy
G	Mass flux
ΔH_f°	Formation enthalpy
h	Step height
h_i	Enthalpy
I_{turb}	Turbulent intensity
N	Total number of species
P	Pressure
Q_{rad}	Radiation
$\dot{r}$	Regression rate
R^2	Coefficient of determination
Re	Reynolds Number
R	Gas constant
T	Temperature
U	Velocity
x/h	Length-to-height ratio
x/l	Step position
y	Mass fraction

ABSTRACT:

In this work, a novel approach to increase the performance of a Hybrid Rocket Engine (HRE) by approximating any idealized fuel port geometry by steps inside the fuel grain is proposed. This work serves as a first investigation into the effect of single steps inside the fuel grains of a typical HRE. In numerical simulations, it is shown that forward- and backward-facing steps have the potential to increase the average regression rate as they promote the turbulence and heat transfer inside the turbulent boundary layer. Both types of steps are more effective at lower oxidizer mass fluxes. Finally, as a first estimation, a set of best practices for the distribution of steps along a profile could be derived.

1. INTRODUCTION

The unique features of Hybrid Rocket Engines (HREs) such as safety and simplicity make them promising candidates for low cost space access. The downsides like low regression rates, slower transients, possibly high fuel slivers and low maturity, however, need to be addressed.

In short, we propose to approximate an idealized fuel port profile by a set of cylinders with different inner diameters (refer to Fig. 1). The flow will therefore display flow phenomena resembling a flow over backward- (BFS) and forward-facing steps (FFS). This way, the engine can profit both from the regression rate enhancement due to the steps, and exhibits the benefits of an idealized profile. Adding to this, the design is easy to manufacture, since there is no need for additive manufacturing of complex port geometries.

In order to elaborate the idea, this article is structured as follows: First, the existing research regarding regression rate enhancement in HREs through steps and diaphragms is briefly collected and analysed. Diaphragms are considered here, because the flow phenomena they induce lie somewhere between a forward- and backward-facing step. The literature review is followed by a numerical study using the multi-physics solver CEDRE of ONERA. Here, the effect of a single step on the flow inside a hybrid rocket combustion chamber is investigated. Furthermore, in evaluating several step configurations such as forward- and backward-facing steps with different heights, an important height-to-length relationship for the recirculation zone can be derived. An extensive case study for a HRE with steps (and its unique interdependence of fuel addition from the fuel surface, mixing, heat transfer and regression rate) is lacking to the knowledge of the authors.

2. THE CONCEPT

Starting point is the fact that the characteristics of HREs can be altered by changing the fuel port profiles. These profiles can be optimized according to different criteria. For example, a genetic algorithm (previously developed at ONERA) [1] can be fed with different optimization criteria (e.g. constant oxidizer-to-fuel ratio or low fuel residuals) to calculate an idealized fuel port profile. However, producing these geometries with conventional fuel casting methods is difficult. Hence, additive manufacturing is often the only possibility to create the desired profiles. Moving to larger scales, this leads to increased complexity and cost. This is where a second observation comes into play. Over the years, several researchers investigated the effect of diaphragms and other obstacles (such as steps) in the HRE combustion chamber. Overall, the results were the same; due to the turbulence and enhanced mixing after the obstacles (introduced by the recirculation zone) the heat transfer and the regression rate increased.

The proposed design approach is therefore the following: If an idealized profile can be approximated by a set of steps (as depicted in Fig. 1), one could theoretically achieve three major advantages: 1) The profile no longer needs to be printed but can be approximated by a finite number of fuel cylinders with different inner diameters. 2) The idealized profile provides the characteristics it was optimized for, e.g. lower O/F shift during operation. 3) Due to the turbulence introduced by the steps, the regression rate and mixing increases. In this paper, the main goal is to derive a set of considerations and guidances on how to best distribute a set of steps along any desired profile. This is done by simulating the impact of single BFS and FFS for different step heights on the fuel surface temperature, regression rate, fuel mass flow and recirculation zone length (RZL). These data allow to understand which is the most efficient way to distribute a set of BFS and FFS along a predefined profile.

3. DIAPHRAGMS AND STEPS IN THE LITERATURE

The concept of steps or diaphragms in the fuel port to promote turbulence and mixing is not new. ONERA employed a diaphragm in the LEX (Lithergol Experimental) rocket in the 1960s [2], making it the first diaphragm in a hybrid rocket motor with flight heritage. Gany and Timnat [3] observed average regression rate increases of 50 % when employing a diaphragm in the middle of their polyester fuel grain already in 1972. Grosse [4] extensively conducted studies on diaphragm form and position in paraffin HREs (a work that has been continued at University of Padua [5]). The common results show regression rate increases downstream the diaphragms by up to 90 % for lab-scale motors and combustion efficiency increases from 76 % to 95 %. Zhang *et al.* [6] pointed out that the regression rate after the diaphragm peaks consistently at the point of the re-attachment of the flow. This effect was exploited by Kumar and Kumar [7] (numerically) and Dinesh and Kumar [8] (experimentally): Both teams placed multiple diaphragms in the fuel grain to further extend the effect of diaphragms. They evaluated that the diaphragms are best to be placed after the recirculation zone of the preceding diaphragm. Quantitatively speaking, for Kumar and Kumar the ideal spacing was 8-10 times the height of the diaphragm in numerical simulations [7], which corresponds to the observed RZL. Interestingly, Dinesh and Kumar observed the optimal spacing to be about 2.7 times of the RZL.

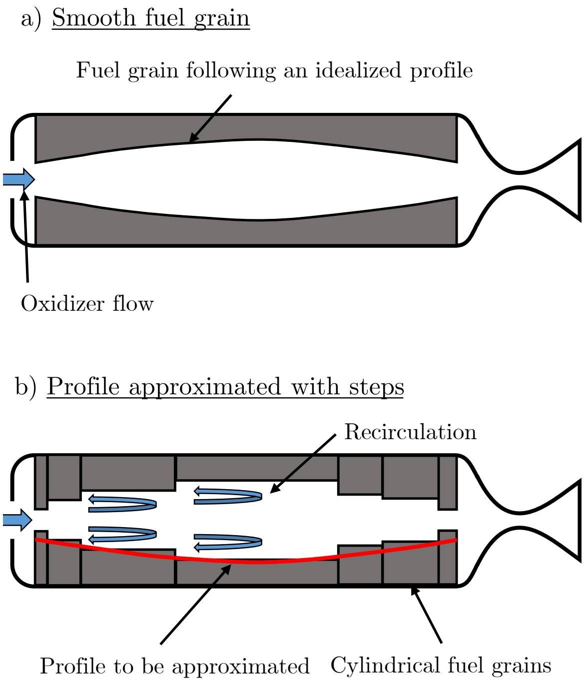

Figure 1: The proposed stepped concept

Concerning the use of steps in HREs, first records of a hybrid rocket motor with a backward facing step can be found in Korting *et al.* [9] in 1987. It was shown that a BFS at the port entrance (hence, technically the step is not inside the fuel grain) doubled the local regression rate after the step. Noteworthy, the peak of the regression rate enhancement appeared at the point of the re-attachment of the flow after the step, as has been pointed out for diaphragms also. Lee *et al.* [10] proposed the use of a backward facing step instead of a diaphragm to avoid the pressure oscillations often induced by diaphragms. The stepped geometry was achieved by combining two fuel grains with different inner diameters. With a 7.5 mm step, the regression rate increased by about 50 % downstream the backward facing step. Sakashi *et al.* [11] used multiple steps with alternating inner diameters. Their so-called concave-convex design effectively resembles a sequence of BFS and FFS with a maximal height difference of 9 mm. In doing so, the regression rate could be increased experimentally by up to 100 %. Kumar and Joshi [12] used 5 cylindrical fuel grains with either 25 mm or 35 mm inner diameter. Combining them, a BFS/FFS fuel port could be created that increased regression rates between 30-50 %. Contrary to the multi-diaphragm research, for steps, the optimal spacing due to the RZL has not been exploited.

Distributing a set of BFS and FFS along an optimized profile has neither been proposed nor investigated. This is where our proposal to distribute a set of BFS and FFS to follow a predefined optimized profile comes into play.

4. NUMERICAL SET-UP

The simulations are carried out with the multi-physics solver CEDRE of ONERA [13]. This section provides a brief overview of the underlying numerical models and assumptions of the hybrid rocket simulations. As this paper is focused on the application of the model rather than the numerical implementation, the concepts are only briefly described. For a detailed and thorough understanding it is highly recommended to refer to the work of Durand *et al.* [14, 15] who implemented the HRE regression rate model into CEDRE. The base-line of the simulation is based on the HYCAT (*Hybride avec CATalyseur*) facilities of ONERA. The HYCAT family uses H_2O_2 and High-Density Polyethylene (HDPE) as propellants. The hydrogen peroxide is decomposed with a catalyst into hot water steam and gaseous oxygen. This is why only the gas phase has to be considered for the simulations, decreasing also the numerical complexity. As for the pyrolysis products of HDPE, only gaseous ethylene (C_2H_4) is assumed. Together with the decomposed hydrogen peroxide this leads to the following chemical species in the simulations: H_2O, CO, CO_2, O_2 and C_2H_4.

Given the significant difference of fuel regression rate (mm/s) and oxidizer flow velocity (m/s), the flowfield is considered as quasi-steady. The simulations are 2D-axisymmetric and the flow is described by the compressible Reynolds-Averaged Navier-Stokes equations. The set of equations is closed with the Shear Stress Transport (SST) model of Menter [16], combining the benefits of the k-ϵ model in the core flow and the k-ω model near the walls. Due to the fuel injection at the fuel surface, the correction of Wilcox [17] for the specific dissipation at the fuel wall is considered. The fuel inlet is modeled with an Gas Surface Interaction (GSI) model using an Arrhenius-type description to calculate the regression rate based on the fuel surface temperature.

4.1. Chemical reaction

The combustion inside an HRE is described by a turbulent diffusion flame. The two-step kinetic chemical reaction denotes according to Westbrook and Dryer to [18]:

$$C_2H_4 + 2O_2 \longrightarrow 2CO + 2H_2O \tag{1}$$

$$CO + 0.5O_2 + H_2O \longleftrightarrow CO_2 + H_2O \tag{2}$$

The detailed rates of production and destruction can be found in Ref. [14].

4.2. Gas-surface interaction model

The GSI model at the fuel surface used in CEDRE of Durand *et al.* [14, 15] is based on an energy- and mass balance at the fuel surface. It allows to couple the fuel surface temperature to the regression rate, allowing to calculate the regression rate rather than fixing it at the fuel surface.

According to mass conservation at the fuel surface, the mass flux of the fuel (G_{fuel}) can be written as:

$$G_{\text{fuel}} = \rho_s \cdot \dot{r} \ , \tag{3}$$

with ρ_s being the solid fuel density and $\dot{r}$ the regression rate. The production rates $\dot{\omega}_i$ of each species i are considered source terms and yield the mass balance:

$$y_i \cdot G_{\text{fuel}} - \rho D_{m,i} \frac{\partial y_i}{\partial \eta} = \dot{\omega}_i \ , \tag{4}$$

with D_m being the diffusion coefficient, y the mass fraction and η the radial coordinate. We consider the sum of the mass source terms $\dot{\omega}_i$ to be equal to the total fuel mass flux and ethylene as the sole pyrolysis product:

$$\sum_{i=1}^{N} \dot{\omega}_i = G_{\text{fuel}} \ . \tag{5}$$

Moreover, the energy balance (gas phase left, solid phase right) denotes to :

$$\begin{aligned} &\lambda_g \frac{\partial T}{\partial \eta} + Q_{\text{rad}} - \sum_{i=1}^{N} \dot{\omega}_i \cdot h_i \\ &= \lambda_s \big(\frac{\partial T}{\partial \eta}\big)_s - G_{\text{fuel}} \cdot h_{\text{fuel}} \ . \end{aligned} \tag{6}$$

$\lambda_{g/s}$:	Thermal conductivity gas/solid
T :	Temperature
Q_{rad} :	Net radiation
h :	Enthalpy
N :	Total number of species

Assuming a quasi-steady heat flux through the solid fuel:

$$\lambda_s \big(\frac{\partial T}{\partial \eta}\big)_s = G_{\text{fuel}} \cdot c_{p,\text{fuel}} \cdot \Delta T \ , \tag{7}$$

Eq. 6 simplifies to (by neglecting radiative heat transfer) [14]:

$$\lambda_g \frac{\partial T}{\partial \eta} = \sum_{i=1}^{N} \dot{\omega}_i \cdot h_i - G_{\text{fuel}} \cdot \Delta H^{\circ}_{f,\text{fuel}} \,, \tag{8}$$

with $c_{p,\text{fuel}}$ and $\Delta H^{\circ}_{f,\text{fuel}}$ being the heat capacity and formation enthalpy respectively. Finally the production rate of ethylene (C_2H_4) – hence the fuel mass flow G_{fuel} – is given by the Arrhenius law:

$$G_{\text{fuel}} = A_{pyr} \cdot \exp\left(-\frac{E_a}{R \cdot T}\right) . \tag{9}$$

The values for the pre-exponent A_{pyr}, the activation energy E_a and the formation enthalpy $\Delta H^{\circ}_{f,\text{fuel}}$ for HDPE are listed in Tab. 1.

Table 1: Properties of HDPE [14]

A_{pyr} $[\frac{kg}{m^2 s}]$	E_a $[\frac{J}{mol}]$	$\Delta H^{\circ}_{f,\text{fuel}}$ $[\frac{J}{kg}]$
$3.5 \cdot 10^6$	$125.6 \cdot 10^5$	$-6.365 \cdot 10^5 \pm 1.14 \cdot 10^4$

4.3. Computational domain

The computational domain in this article is based on the HYCAT facilities at ONERA, allowing to be able to validate the simulations and their continuation in the future. In order to decrease the number of influences on the results of the fuel surface, at this stage of the research the HYCAT family is approximated by a 2D axisymmetrical academic domain, as depicted in Fig. 2 for the BFS case. The open source software GMSH is used to create the meshes. The total fuel grain length is 240 mm. The inlet fixes the oxidizer mass flux (G_{ox}) and the inlet temperature. The fuel surface is modeled according to the GSI presented in Sec. 4.2 and the outlet is a pressure outlet which fixes the pressure to a value representative to a nozzle. The mesh is chosen to be Cartesian because it lessens the number of cells (as compared to triangles) and allows to refine the mesh size close to the fuel surface to approximate the boundary layer region. The minimal cell size at the fuel surface is calculated to ensure an $y+ < 1$ for all possible total cell counts. The inner diameter before the step is fixed to 25 mm as this represents the minimum diameter of HYCAT. The diameter after the step is dependent on the step height (h). For a maximum step size of 10 mm this leads to a diameter after the step of 45 mm.

Changing from BFS to FFS domain is conveniently achieved by switching the inlet and outlet conditions. This signifies that for the FFS cases, the diameter after the step is always fixed to 25 mm and the diameter before the step changes according to the step height. Translated to a real world application this means that a cylindrical fuel grain with two different inner diameters is simply turned around.

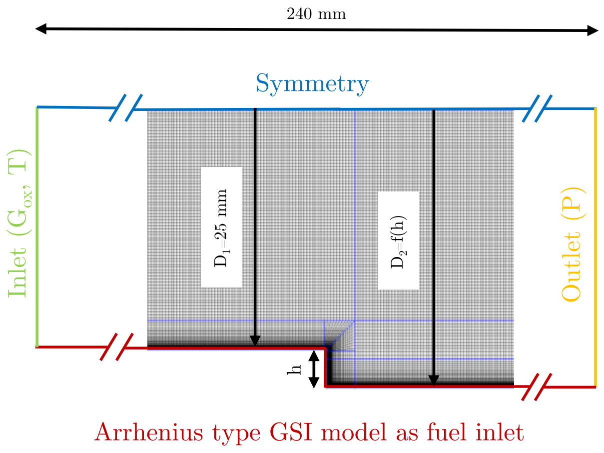

Figure 2: Computational domain for BFS case

4.4. Mesh convergence

Since at this stage of the research we are not yet able to validate the simulations experimentally, it is of upmost importance to prove that the results are independent from the mesh. In order to do so, six different meshes with increasing cell count (from roughly 15,000 to over 400,000) are created for a BFS domain with a step height of 2 mm. All meshes ensure a $y+ < 1$ at the fuel surface. The results are presented in Tab. 2. Mesh 1 (14,902 cells) serves as starting point and the cell count is approximately doubled with each mesh. After each individual simulation is converged, the average values of surface pressure, surface temperature, total fuel mass flow and RZL are gathered for 10,000 iterations with 100 data points for the same physical time. Mesh 1 presents the base case, the values for meshes 2-6 give the relative change compared to the preceding simulation. For example, for mesh 4, the total fuel mass flow increased by 0.16 % as compared to the fuel mass flow of mesh 3. The boundary conditions of the mesh convergence study are loosely based on the conditions inside a typical HYCAT firing and can be found in Tab. 3.

Looking at Tab. 2, it becomes obvious that the average values of pressure and temperature converge very fast and could be considered mesh independent starting from mesh 1. For the fuel mass flow, however, the values can be considered convergent somewhere between mesh 2 and 3. The largest changes in values can be seen for the RZL. After the first refinement to mesh 2, the length of the recirculation zone increased by almost 20 %. This is due to the fact that the coarse mesh 1 is not able to properly capture the eddies that are separating after the step. After mesh 3, the RZL finds a more stable value. However, in order to correctly judge the mesh independence for the RZL, it is necessary to also consider the shape of the recirculation zone. Fig. 3 depicts the appearance of the recirculation zone for Meshes 1,4 and 5. It becomes apparent

Table 2: Mesh convergence study

Mesh no.	Cell count	Pressure [Pa]	Temperature [K]	Fuel mass flow [g/s]	Recirculation zone [mm]
1	14,902	3,602,121	924.74	5.978	8.56
2	26,199	+0.025 %	+0.139 %	+2.11 %	+19.77 %
3	56,263	+0.027 %	+0.032 %	+0.56 %	+2.91 %
4	96,683	-0.0002 %	+0.011 %	+0.16 %	+3.77 %
5	208,307	+0.013 %	+0.051 %	+0.9 %	-2.73 %
6	412,097	-0.004 %	+0.017 %	+0.6 %	+1.87 %

Table 3: Boundary conditions of mesh convergence

T_{inlet}	P_{outlet}	G_{ox}	y_{H2O}	y_{O2}	I_{turb}
1000 K	36 bar	$200\frac{kg}{m^2 s}$	0.59	0.41	1 %

that the RZL for case 1 is not at all developed and too short. For mesh 4, however, the length and the height of the RZL seems to have a more consistent appearance. Nonetheless, a smaller second recirculation zone inside the bigger zone is observable, which could have a non-negligible effect on the simulations. Moreover, the contour of the flame zone is less consistent as compared to mesh 5. Mesh 6 only changes the RZL by under 2 %, but uses double the cells. For this reason, mesh 5 with 208,307 cells is considered as the most suitable mesh for the numerical test campaign in terms of mesh independence and computational cost.

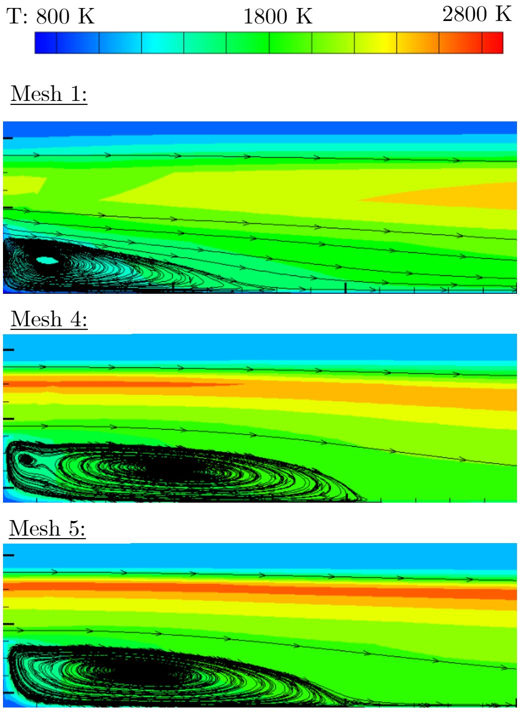

Figure 3: Recirculation zone after the step for different meshes

5. RESULTS AND DISCUSSION

First, the test matrix and the decision process of the boundary conditions are explained. In a next step, the outcome of the simulations is presented and explained. The results to be exploited are: a) Temporal and spatially averaged regression rates. b) Temperature and regression rate profiles in axial direction at the fuel surface. c) Height-to-length relationship for the RZLs.

Before going into the details of the results, we present in short the basic characteristics of the flow phenomena of a flow over a BFS and FFS respectively. Fig. 4 shows the temperature fields and velocity streamlines for a representative flow without step, a BFS with 5 mm height and a FFS with 5 mm height. For the BFS case, the flame zone detaches after the step and re-attaches after the recirculation zone. The flow before the step is unaltered. For the FFS case, however, the step already lifts up the flame zone the closer it gets to the step and a first recirculation zone is already formed before the step. After the step, the flow re-attaches considerably faster than for the BFS case. This is due the fact that in the BFS case, the diameter increases and therefore the flow velocity decreases for a constant mass flow. In the case of the FFS, on the other hand, the diameter decreases and the flow accelerates. This fundamental difference has to be kept in mind when discussing the flow phenomena in the succeeding sections.

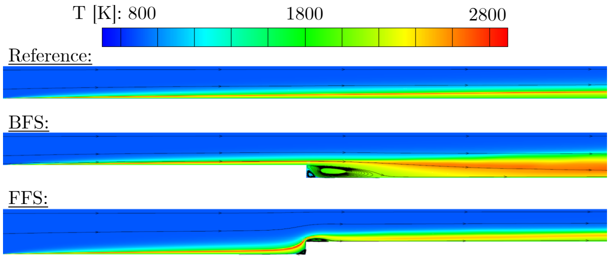

Figure 4: Temperature contours of axisymmetric HRE simulation

5.1. Test matrix

The simulations will be carried out on the domain displayed in Fig. 2. The boundary conditions are being held close to the HYCAT data. Using only a single step at this stage allows to single out the effects of the steps. The interactions between multiple steps will be considered in future work. The following major investigations need to be carried out:

1. **Height study:**
   The impact on different step heights h.
2. **Position study:**
   The effect of the axial position of the step (x/l).
3. **Mass flow study:**
   The importance of the oxidizer mass flux $G_{ox} = \frac{\dot{m}}{A}$ given by the mass flow $\dot{m}$.

These studies are carried out both for the BFS and FFS cases. Between the three different parametric campaigns, all other values are being held constant. The different inlet conditions, step heights and positions can be found in Tab. 5, the boundary conditions (based on typical HYCAT firings) that are similar throughout all calculations are listed in Tab. 4. The results of all studies are collected and their impact on the average regression rate, recirculation zone and temperature and regression rate profiles assessed in the respective subsections.

Table 4: Constant boundary conditions

T_{inlet}	P_{outlet}	$y_{H2O,\text{inlet}}$	$y_{O2,\text{inlet}}$	I_{turb}
900 K	36 bar	0.59	0.41	11 %

5.2. Backward facing step cases

In the following section, first the BFS cases are analyzed separately.

5.2.1. Average regression rate

Fig. 5 depicts the spatially and temporal averaged regression rate values for the BFS cases limited to behind the step. It allows to evaluate the impact of all parametric studies in one single image. The green graph represents the reference cases without any step. The blue line and the crosses correspond to the average regression rate values downstream the step. The label *S2* i.e. corresponds to a step height of 2 mm, the label *S5 end* refers to the case of 5 mm step height at the position $x/l = 0.75$. Additionally, the Marxman [19] fit is given as

$$\dot{r} = a \cdot G_{ox}^{n} \tag{10}$$

where a and n are parameters used to best fit the data points. For the Marxman fit, only the data points of the mass flow study are considered. This allows to extrapolate approximated values even outside of ranges that have been simulated.

Comparing the Marxman fits of the reference cases and the BFS cases, the most prominent observation is that the average regression rate of the BFS cases is inferior at mass fluxes above approximately 100 kg/m^{2}s. Below this value, the average regression rate behind the step is higher than the reference cases without step. Moreover, the cases *S1*, *S2*, and *S5 end* are below the reference cases; whereas the cases *S10* and *S5 front* are above the reference cases. This observation hints at the existence of two competing effects: Directly after the BFS, the flame zone is further from the fuel surface, therefore decreasing the fuel surface temperature. On the other hand, the step introduces a recirculation zone that promotes mixing and heat transfer. If the recirculation zone is too small (as it seems to be the case for 1 mm and 2 mm for higher mass fluxes), the regression rate after the steps never recovers from the flame zone being further from the fuel surface directly after the step. This is also why the case of *S5 front*, where the step is positioned at the beginning of the fuel port rather than the middle, is superior to the references cases: The turbulence induced by the step has more time and space to compensate the decrease of the surface temperature directly after the step. In order to discuss this effect we introduce the temperature and regression rate surface profiles of the different cases in the next part.

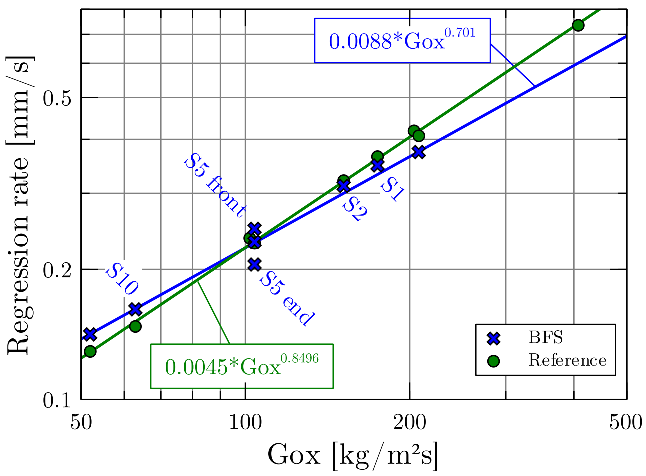

Figure 5: Regression rate after step for BFS

5.2.2. Surface profiles

Fig. 6 shows the temperature distribution along the fuel port surface along the x-axis of the fuel port. Moreover, the gray boxes indicate the length of the recirculation zone induced by the step. The green dotted line specifies the profile of the respective reference cases. Keeping in mind that the diameter of the fuel port increases after the step, we need to consider a different reference case after the step than before. For example, with a mass flow of 100 g/s in a 5 mm case, the reference G_{ox} before the step yields 203 kg/m^{2}s. After the step it decreases to around 104 kg/m^{2}s due to the larger diameter. The step position is at 0 m distance.

With the help of these surface profiles, the aforementioned competing effects of recirculation

Table 5: Values for parametric studies

Study	h [mm]	x/l [-]	$\dot{m}$ [g/s]	Labels
Height	[1, 2, 5, 10]	0.5	100	[S1, S2, S10]
Position	5	[0.25, 0.5, 0.75]	100	[S5 front, S5 end]
Mass	5	0.5	[50 , 100, 200]	none

zone and flame distance from the surface becomes clearer: In all cases, the surface temperature directly after the step drops significantly, given that the flame is further from the surface. However, the surface temperature increases exactly until the re-attachment point (after the recirculation zone). From there on, the heat transfer and the mixing is increased, clearly visible in steeper temperature profiles as compared to the reference case. With the help of Fig. 6 it can be explained why the cases for *S1* and *S2* are inferior to the reference cases: The increased heat transfer induced by the step is too small to compensate the loss of surface temperature directly after the step. Starting with *S5*, the augmented heat transfer is considerably higher than the loss of temperature immediately after the step and can in total increase the surface temperature.

Fig. 7 displays the regression rate profiles of the same cases as Fig. 6. The regression rate profiles follow the exact same trend as the temperature profiles. This is little surprising given that the surface temperature was modeled in the GSI (recall also Sec. 4.2) to be the main influence of the regression rate. Knowing this, we will continue from here on to only consult the regression rate profiles for the sake of efficiency. The regression rate profiles confirm the competing effects: Directly after the step, the regression rate descends well below the reference value. At the re-attachment point, the regression rate peaks (an effect also observed by Refs. [3, 6, 9]) and after a smaller rebound continues with a steeper profile than the reference cases. The effect of the steeper profile can be further illustrated with the results of the step position study in Fig. 8. Here, the step height is constant at 5 mm but the position moved from 25 % (front) to 75 %

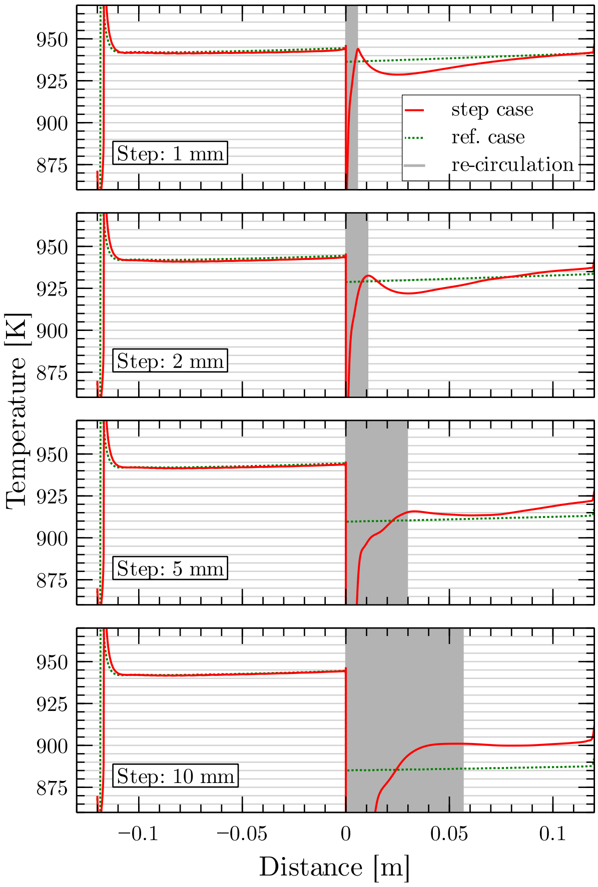

Figure 6: Temperature of the BFS height study

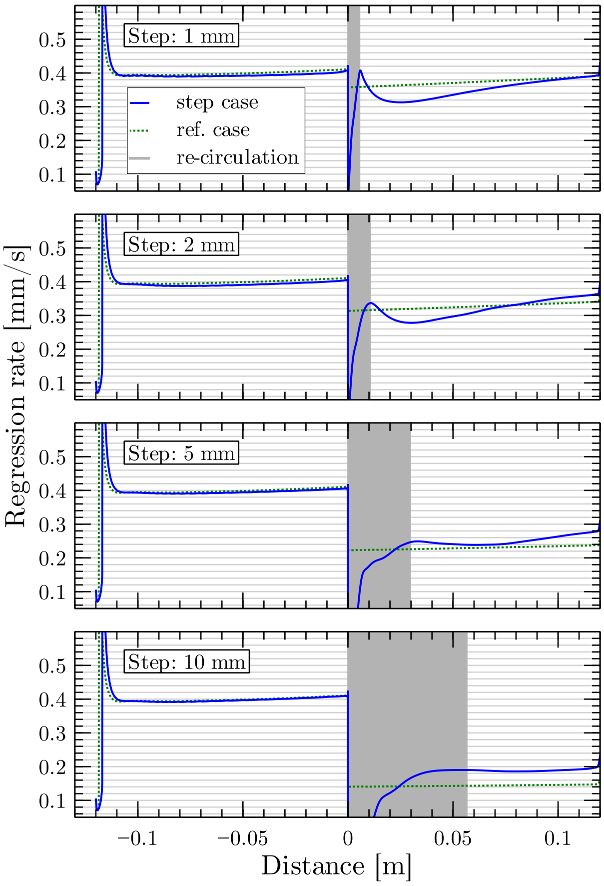

Figure 7: Regression rate of the BFS height study

(end) of the total grain length. It becomes apparent that a BFS at 75 % of the grain length diminishes the effect of the step. Contrarily, for a BFS at 25 %, the steeper regression rate profile considerably increases the regression rate for over the half of the total fuel grain. This explains also why the spatially averaged regression rate of the *S5 front* case in Fig. 5 is superior to the other *S5* cases.

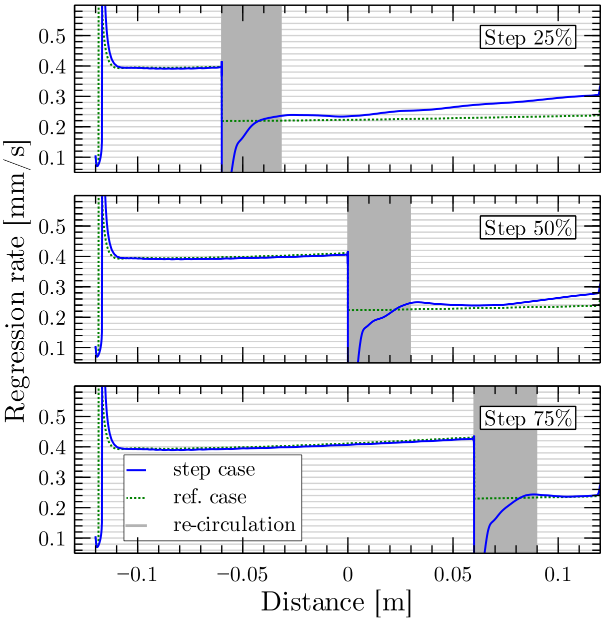

Figure 8: Regression rate profile for different step positions. The step height is constant at 5 mm.

5.2.3. Regression rate for averaged mass flux

To conclude the investigation of the BFS simulations, we draw another comparison to the reference cases using the spatial and temporal averaged regression rate. This time, however, we also average the mass flux for the BFS cases. As known, the mass flux G_{ox} is given by the mass flow $\dot{m}$ and area A as:

$$G_{ox} = \frac{\dot{m}}{A} = \frac{\dot{m}}{0.25 \cdot \pi \cdot D^2} \,. \tag{11}$$

For stepped cases like the BFS and FFS cases, the diameter changes after the step. That is why we define an average mass flux $G_{ox,\text{avg}}$ as:

$$G_{ox,\text{avg}} = \frac{\dot{m}}{A_{avg}} \,, \tag{12}$$

where the average area A_{avg} depending on the step position (x/l) is defined as:

$$A_{avg} = 0.25 \cdot \pi \cdot [(x/l) \cdot D_1^2 + (1 - (x/l)) \cdot D_2^2] \tag{13}$$

with D_1 and D_2 being the diameter before and after the step respectively. With this expression we can now compare the temporal and spatial averaged regression rate of the whole domain with the references case. Fig. 9 illustrates the results. The overall trend is similar to Fig. 5, nonetheless, the average mass flux where the BFS cases become superior to the reference moves up to around 130 kg/m^{2}s. It becomes apparent that lower mass fluxes and step heights of 5 mm and higher yield the best results, while the position of the step should be as early as possible.

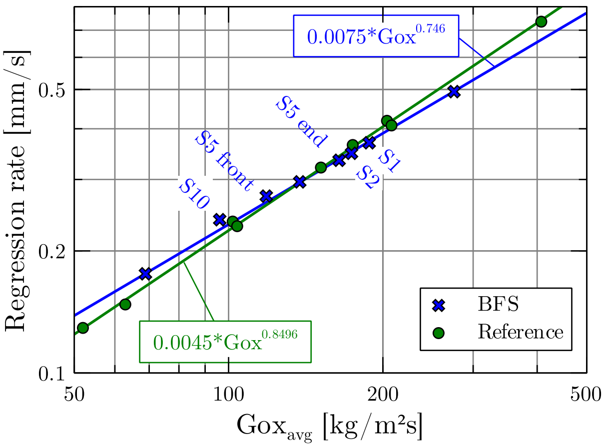

Figure 9: Regression rate of averaged mass flux

5.3. Forward facing step cases

Following the same procedure as for the BFS cases, this section discusses the outcome of the FFS simulations.

5.3.1. Average regression rate

Fig. 10 reports the average regression rate behind the FFS in red and compares them to the reference cases without a step. The prominent observation is that – contrary to the BFS cases – all FFS cases exhibit a higher regression rate than the reference cases. However, the difference declines with increasing mass flux. Preliminary, this leads to the conclusion that FFS are better suited to increase the regression rate through turbulence and enhanced heat transfer than BFS. This conclusion will be elaborated further in the next section when looking at the surface profiles. The reason why most of the FFS cases are clustered at the same G_{ox} value is that for the FFS domain, the diameter after the step is fixed to 25 mm, whereas the diameter before the step changes depending on the step height. That is why in Fig. 11 a more detailed view of the area labeled *Detail A* is provided.

Here, it is to be noted that the *S1* case has about the same regression rate as the reference cases. Starting with *S2*, the difference grows. Interestingly, there seems to be a negligible difference between the *S5* and *S10* cases. A trend opposite to the BFS cases where the *S10* BFS was by far superior to all other cases. Moreover, for the BFS cases, the regression rate was highest when the step position is in the front. For the FFS, on the other hand,

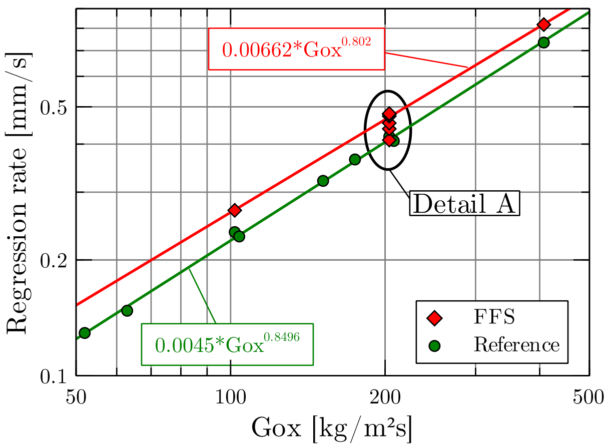

Figure 10: Regression rate after step for FFS

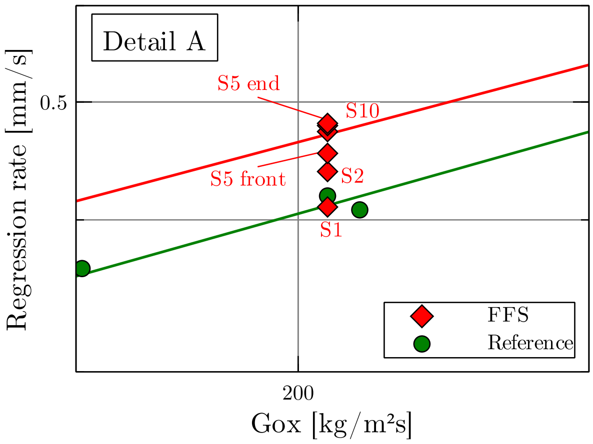

Figure 11: Detail A of regression rate after FFS

the step position at the end exhibits the highest regression rate. This observation will also be further investigated with the help of the surface profiles in the next section.

5.3.2. Surface profiles

Before taking the surface profiles into account, it is reminded that we will concentrate solely on the regression rate profiles. This decision is justified, since we showed in the BFS section that the temperature and the regression rate profiles follow the exact same trend, as it is expected from the implementation of the Arrhenius law in the GSI. Likewise to the BFS surface profiles, Fig. 12 compares the regression rate to the reference cases while indicating also the RZLs. Due to the diameter being smaller after the step (leading to increased G_{ox}) the reference cases before and after the step are different in order to refer to the proper mass flux.

The first observation is that contrary to the BFS cases, the influence of the FFS is already noticeable before the step. This is due to the step 'pushing' the flame further away from the surface the closer it gets to the step. As soon as the recirculation zone before the step is reached, the regression rate drops drastically. This leads to an overall smaller regression rate before the step as compared to the reference cases. For the 10 mm case, this effect is the most visible. After the step, the regression rates show a steep increase with a distinct peak exactly at the re-attachment point. For the BFS cases, this peak was visible, but less pronounced. Moreover, for the BFS cases, the recirculation zone is considerably larger than for the FFS cases. This translates to the regression rate peak being reached earlier than for the BFS cases. After the peak, the regression rate follows approximately the same angle as the reference case. Interestingly, the difference between the 5 mm and 10 mm step is almost negligible after the step, whereas the negative effects before the step itself are considerably higher. This leads to the conclusion that the the FFS should not be higher than 5 mm. Another fundamental differences to the findings of the BFS cases, where the 10 mm case is to be preferred.

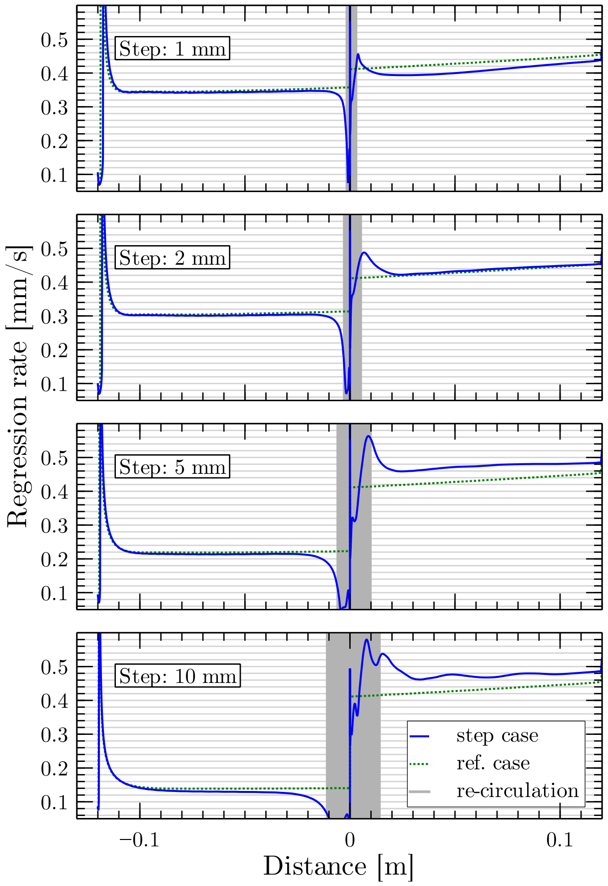

Figure 12: Regression rate of the FFS step height study

If we turn now to the step position study that is detailed in Fig. 13, we can observe another discrepancy to the BFS cases: For the FFS cases, the step position further downstream increases the regression rate the most. At the 25 % position, the peak is not only smaller but also less pronounced. Additionally, the decrease in regression rate before the step is noticeable already before the recirculation zone starts. Given that the turbulent boundary layer and its flame zone is less developed at the 25 % position, we can assume that the disturbance of the flow at the earlier position is stronger.

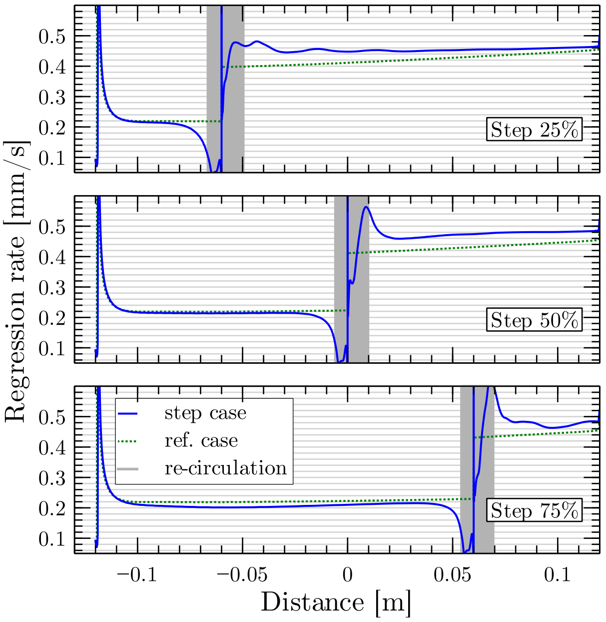

Figure 13: Regression rate profile for different step positions. The step height is constant at 5 mm.

5.3.3. Regression rate for averaged mass flux

Following Eq. 12 that was derived to average the mass flux not only after the step but over the whole domain, Fig. 14 displays the averaged regression rate over the average mass flux. In line with Fig. 10, nearly all FFS cases are superior to the reference cases. Additionally, the effect increases with decreasing mass flux. Unexpectedly, the *S5 end* case drops below the expected trend of the FFS Marxman fit, although in Fig. 13 this case seemed superior. Since the step in this case is at 75 % of the total canal length, the increased regression rate after the FFS only contributes to 25 % of the total canal length. Therefore the disturbances at 75 % of the total length caused before the step dominates during the averaging process. Nonetheless, the *S5 end* case lies still above the reference cases.

5.4. Height-to-length relationship

In this section, we put the length of the recirculation zone (x) in relation to the height of the step (h) that is inducing the recirculation zone. This yields the height-to-length relationship x/h. In order to compare the different relations amongst each other, we introduce the step Reynolds number Re_h, following a common approach in the literature [20, 21]:

$$Re_h = \frac{U \cdot \rho \cdot h}{\mu}\,, \tag{14}$$

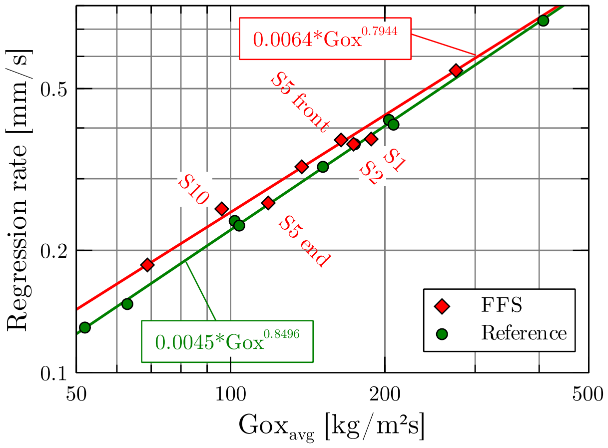

Figure 14: Regression rate of averaged mass flux

with U being the free stream velocity, ρ the flow density and μ the dynamic viscosity. All values are calculated at the domain inlet. Fig. 15 displays the RZL for the BFS case. For the FFS, the two recirculation zones (before and after the step) are given. Additionally, a power law fit is plotted for each data-set and the coefficient of determination (R^2) specified. The values of the BFS recirculation zones lie between 4.9 and 6.9 and their evolution is coherent with the trends that are found in (non-HRE) literature of BFS flows (eg. Ref. [20]): With increasing Re_h, the x/h ratio increases and shows saturating behaviour. This also can serve as one possible explanation why the BFS cases benefit from lower mass flows and thus, lower Re_h values. The regression rate for BFS cases has shown to be inferior to the reference cases within the recirculation zone. It is typically after the recirculation zones that the regression rate overtakes the reference cases (refer to Fig. 7). Hence, with smaller recirculation zone relative to the step height, the BFS cases become more competitive. Given that the x/h decreases with decreasing mass flow, this could be an explanation for the trend.

For the x/h ratio before the FFS, the trend also is well in line with what is reported in (non-HRE) FFS literature [21]: With increasing mass flow and Reynolds number, the recirculation zone ratio before the FFS step decreases. Unexpectedly, the data for the x/h ratio after the FFS is inverse to what is found in (non-HRE) literature [21]. Literature reports the x/h after the FFS to increase with the Reynolds number. However, for our FFS cases, the ratio decreases with increasing Reynolds number. The reason for this behaviour could not be fully understood yet and is part of on-going investigations in the future. One possible explanation can be the differences between the cases in the literature and our HRE related set-up. For example, in the FFS literature, usually the flow is not axisymmetric but on flat surfaces. In the HRE FFS case, we have an axisymmetric geometry, where the flow significantly accelerates after the FFS due to the smaller diam-

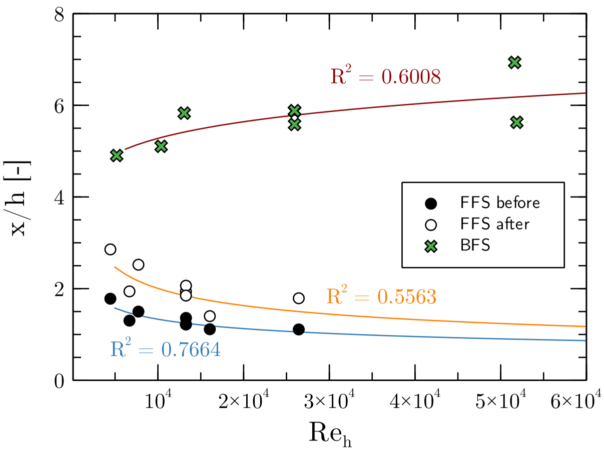

Figure 15: Length-to-height ratio of recirculation zones

eter. Moreover, according to the Marxman law, the regression rate increases with increasing mass flux after the FFS. This leads to increased blowing from the surface, especially at the end of the recirculation zone where a pronounced peak of regression rate was observable. All these alterations to the typically planar literature case could serve as explanation for the discrepancy of the (non-HRE) literature and our results.

6. CONCLUSION AND OUTLOOK

In this work, we proposed a novel approach to increase the performance of HREs. The concept is to approximate any idealized profile inside a fuel port with a set of BFS and FFS (recall also Fig. 1). This way, potentially, the engine can profit from the idealized fuel profile, while also exhibiting higher regression rates due to the turbulence inducing steps. Since there is few available data on the effects of BFS and FFS in HREs, the first step to promote the idea was to understand the effect of single steps on the regression rate. These results will build the foundation of future algorithms to distribute multiple steps. Hence, the following main observations are to be recalled:

1. FFS cases exhibit in all but one case higher regression rates than the non-step references.
2. BFS cases are assumed to have a 'break-even' point (below around 130 kg/m^{2}s oxidizer mass flux) where they are superior to the reference cases.
3. Both BFS and FFS have shown to be more effective with decreasing oxidizer mass flux.
4. In all cases, the peak in regression rate was observed to be at the re-attachment point.
5. For BFS, the higher the step, the better the regression rate enhancement; for FFS, the augmentation has shown to be saturated for 5 mm step height.
6. For BFS cases, the regression rate increases more after the recirculation zone than within, that is why a step at the beginning of the fuel port yielded better results than at the other positions downstream. This trend is considerably less pronounced for FFS, and might even be inverse.

Concluding these investigations, a first careful conclusion can be drawn, serving as an initial best practice for the distribution of steps along an approximated profile: It is advised to use fewer but taller and longer BFS, preferably upstream the fuel port, while the height of the FFS should be limited to 5 mm. FFS are less susceptible to its length and axial position inside the fuel port.

For the future, it is necessary to validate these first findings not only numerically but also experimentally. Moreover, this work has been concentrated solely on single steps. It is of importance to confirm the results for multiple steps and validate if the interaction of several steps is benefiting the regression rate increase or maybe even diminishing it. Another concern is the evolution of the steps with time. If the steps dissolve rapidly as the burn continues, the turbulence enhancing effects would also get lost. Nonetheless, the profile that was once approximated by steps would be now smooth and could still benefit from the profile optimization (while it was less complex to manufacture as compared to printed solutions). This will be investigated in continuation of this work.

In conclusion, we have demonstrated that BFS and FFS have a turbulence and regression rate enhancing effect on HREs and can thus be potentially used to approximate fuel port geometries. The results of the parametric study will serve as a starting point to develop an algorithm to distribute steps along an idealized profile. Even though the research is still in an early stage, we believe that BFS and FFS can be a promising addition to HREs, especially when they are used to minimize manufacturing effort while also increasing the performance.

ACKNOWLEDGEMENTS

The authors would like to thank Dr. Levard for his guidance on CEDRE and the meshing of the computational domain.

The project leading to this application has received funding from the European Union's Horizon 2020 research and innovation programme under the Marie Sklodowska-Curie grant agreement No 860956. It is part of the ASCenSIon project, an Innovative Training Network (ITN) to advance space access capabilities.

References

[1] J. Hijlkema, “A presentation of a complete design cycle for optimised hybrid rocket motors,” in *SpacePropulsion 2018, Seville*, 2018.

[2] P. Duban, “La fusée sonde lex,” *Extrait de l’Aéronautique et l’Astronautique*, no. 2, 1968.

[3] A. Gany and Y. Timnat, “Parametric study of a hybrid rocket motor,” *Israel Journal of Technology*, vol. 10, pp. 85–96, Jan. 1972.

[4] M. Grosse, “Effect of a diaphragm on performance and fuel regression of a laboratory scale hybrid rocket motor using nitrous oxide and paraffin,” in *45th AIAA/ASME/SAE/ASEE Joint Propulsion Conference and Exhibit*, (Reston, Virginia), American Institute of Aeronautics and Astronautics, Aug. 2009.

[5] N. Bellomo, M. Lazzarin, F. Barato, A. Bettella, D. Pavarin, and M. Grosse, “Investigation of effect of diaphragms on the efficiency of hybrid rockets,” *Journal of Propulsion and Power*, vol. 30, pp. 175–185, Jan. 2014.

[6] S. Zhang, F. Hu, D. Wang, P. Okolo.N, and W. Zhang, “Numerical simulations on unsteady operation processes of N2O/HTPB hybrid rocket motor with/without diaphragm,” *Acta Astronautica*, vol. 136, pp. 115–124, 2017.

[7] C. P. Kumar and A. Kumar, “Effect of diaphragms on regression rate in hybrid rocket motors,” *Journal of Propulsion and Power*, vol. 29, pp. 559–572, May 2013.

[8] M. Dinesh and R. Kumar, “Utility of Multiprotrusion as the Performance Enhancer in Hybrid Rocket Motor,” *Journal of Propulsion and Power*, vol. 35, pp. 1005–1017, July 2019.

[9] P. A. O. G. Korting, H. F. R. Schöyer, and Y. M. Timnat, “Advanced hybrid rocket motor experiments,” *Acta Astronautica*, vol. 15, pp. 97–104, Feb. 1987.

[10] J. Lee, S. Rhee, J. Kim, H. Moon, O. Shynkarenko, D. Simone, and T. Morita, “Combustion instability for hybrid rocket motors with a diaphragm,” *Proceedings of the 8th European Conference for Aeronautics and Space Sciences. Madrid, Spain, 1-4 July 2019*, 2019.

[11] H. Sakashi, Y. Saburo, H. Kousuke, and S. Takashi, “Effectiveness of Concave-convex Surface Grain for Hybrid Rocket Combustion,” *48th AIAA/ASME/SAE/ASEE Joint Propulsion Conference and Exhibit*, July 2012.

[12] M. Kumar and P. Joshi, “Regression rate study of cylindrical stepped fuel grain of hybrid rocket,” *Materials Today: Proceedings*, vol. 4, no. 8, pp. 8208–8218, 2017.

[13] A. Refloch, B. Courbet, A. Murrone, P. Villedieu, C. Laurent, P. Gilbank, J. Troyes, L. Tessé, G. Chaineray, J. Dargaud, E. Quémerais, and F. Vuillot, “Cedre software,” *AerospaceLab Journal*, 03 2011.

[14] J.-É. Durand, F. Raynaud, J.-Y. Lestrade, and J. Anthoine, “Turbulence Modeling Effects on Fuel Regression Rate in Hybrid Rocket Numerical Simulations,” *Journal of Propulsion and Power*, vol. 35, pp. 1127–1142, Nov. 2019.

[15] J.-E. Durand, *Développement et validation expérimentale d’une modélisation numérique pour la simulation d’un moteur-fusée hybride*. PhD thesis, Universite de Toulouse, 2019.

[16] F. R. Menter, “Two-equation eddy-viscosity turbulence models for engineering applications,” *AIAA Journal*, vol. 32, pp. 1598–1605, Aug. 1994.

[17] D. C. Wilcox, “Reassessment of the scale-determining equation for advanced turbulence models,” *AIAA Journal*, vol. 26, pp. 1299–1310, Nov. 1988.

[18] C. K. Westbrook and F. L. Dryer, “Simplified reaction mechanisms for the oxidation of hydrocarbon fuels in flames,” *Combustion Science and Technology*, vol. 27, no. 1-2, pp. 31–43, 1981.

[19] G. Marxman and M. Gilbert, “Turbulent boundary layer combustion in the hybrid rocket,” *Symposium (International) on Combustion*, vol. 9, pp. 371–383, Jan. 1963.

[20] L. Chen, K. Asai, T. Nonomura, G. Xi, and T. Liu, “A review of Backward-Facing Step (BFS) flow mechanisms, heat transfer and control,” *Thermal Science and Engineering Progress*, vol. 6, pp. 194–216, June 2018.

[21] M. Awasthi, W. J. Devenport, S. A. L. Glegg, and J. B. Forest, “Pressure fluctuations produced by forward steps immersed in a turbulent boundary layer,” *Journal of Fluid Mechanics*, vol. 756, pp. 384–421, Oct. 2014.